Water Resources Research

Supporting Information for

Diurnal to Seasonal Dynamics of Groundwater, Evaporation, and Hydrology Fluctuations at the Bonneville Salt Flats Saline Pan

BJ.A. Bernau[1], B. B. Bowen[1,2], E. R. Pardyjak[3], and E. L. Kipnis[1]

[1]Geology and Geophysics, University of Utah, Salt Lake City, UT, USA; [2]Global Change and Sustainability Center, University of Utah, Salt Lake City, UT, USA; [3]Mechanical Engineering, University of Utah, Salt Lake City, UT, USA

Contents of this file

Text S1 to S3
Figures S1 to S9

Introduction

This file contains supporting information describing data sources, data processing steps, and theoretical background, as well as supplemental figures. The data quality control, gap-filling, and Matlab (MathWorks, 2020b) analyses code used for this study is available at https://doi.org/10.5281/zenodo.5671739 and the datasets that support this work are archived at https://doi.org/10.5281/zenodo.5634172 and https://doi.org/10.5281/zenodo.4268710. These datasets consist of modern and historical meteorological and groundwater measurements.

Supporting Information

Text S1. Meteorological Data

Meteorological measurements and products are archived at https://doi.org/10.5281/zenodo.5634172. The data quality control, gap-filling, and Matlab (MathWorks, 2020b) analyses code used for this study are archived at https://doi.org/10.5281/zenodo.5671739.

Meteorological measurements and surface observations

Historical meteorological measurements from the Bonneville Salt Flats and the surrounding area were reported by Lines (1979) and Mason and Kipp (1998). Additional measurements from Wendover, Utah, were collected from the National Oceanic and Atmospheric Administration (NOAA) Climate Data Online Portal. Weather station data at BSF was collected from the MesoWest weather station data repository (https://mesowest.utah.edu/, station ID: BFLAT) (Horel et al., 2002).

These measurements were used to examine the spatial and temporal heterogeneity of precipitation and evaporation in the area surrounding BSF (Figure S2). Precipitation in 2020 was four times lower than the preceding years of 2017 to 2019. The year of 2019 was 40% wetter than the next wettest year during the study period of 2016 to 2021.

Eddy-Covariance Data and Aerodynamic Roughness

The eddy-covariance equipment was oriented to the northwest and installed at the height of 2.57 m from May to August 2018. Eddy-covariance data available at https://doi.org/10.5281/zenodo.5634172 and the code used to determine the aerodynamic roughness length is available at https://doi.org/10.5281/zenodo.5671739.

The aerodynamic roughness length (Z_o) (meters) was determined with sonic anemometer data collected from May to August 2018 with equation S1-1. Equation S1-1 is rearranged to solve for Z_o in equation S1-2; the data is filtered where L is > 100 m, such that $\Psi_m(\frac{Z}{L})$ approaches zero (Stull, 2012).

$$\frac{\overline{m}}{u_*} = 1/K(\ln\left(\frac{Z}{Z_o}\right) + \Psi_m\left(\frac{Z}{L}\right)) \quad \text{(S1-1)}$$

$$Z_o = Z/\exp\left(K\frac{\overline{m}}{u_*}\right) \quad \text{(S1-2)}$$

Where $\overline{m}$ is wind speed (m/s) filtered to only include wind speeds between 2-6 m/s, μ_* is the friction velocity (m/s), K is the von Karman Constant (0.4), Z is the measurement height (m), Ψ_m is the stability function, and L is the Monin-Obukhov length scale. The median value of Z_o at BSF was $5.4*10^{-4}$ m.

Meteorological data gap filling

Outgoing and net longwave radiometer measurements from November 24, 2019 to March 2, 2020 were removed from the dataset for quality control. Longwave radiation measurements were not available prior to the installation of the longwave radiometers on June 6, 2017. An artificial neural network was shown to estimate radiation effectively by Kelley (2020). The neural network (using the methods outlined in Text S3, and with the training inputs of air temperature, relative humidity, wind speed, incoming and outgoing shortwave radiation, and time of day) was used to fill data

gaps. The artificial neural network was more effective at estimating net longwave radiation than incoming longwave radiation (Figure S3). Incoming longwave radiation was calculated by subtracting the outgoing radiation from net longwave radiation.

From June 9 to 11, 2019, the weather station did not log meteorological measurements. Temperature, humidity, air pressure, and incoming shortwave radiation measurement from this period were replaced with measurements made by the nearby DPG17 weather station (https://mesowest.utah.edu/, station ID: DPG17). Outgoing shortwave radiation and incoming and outgoing longwave radiation during this period were replaced with measured mean BSF radiation measurements from the preceding and proceeding days.

Imagery

The saline pan's surface properties and surface features changed over time with evaporite growth, dissolution, and alteration. Time-lapse imagery from the BFLAT weather station is available at http://home.chpc.utah.edu/~u0790486/wxinfo/cgi-bin/uunet_camera_explorer.cgi Camera: Bonneville Salt Flats, and, along with imagery from other locations at https://doi.org/10.5281/zenodo.4171331 (Bernau & Bowen, 2021). There are some gaps within the weather station-collected imagery because of equipment malfunctions. The camera view was shifted downward from April 7 to 11, 2018. The camera was non-functioning from February 7 to May 18, 2020.

Text S2. Estimated Evaporation Models

Estimated evaporation model results are available at https://doi.org/10.5281/zenodo.5634172 and code is available at https://doi.org/10.5281/zenodo.5671739.

Potential evaporation-based models

Water Activity

The water activity of BSF brines was estimated with geochemical modeling and previously derived empirical relationships between brine density and water activity for BSF brines (Turk, 1973). Water samples from BSF (Kipnis et al., 2020) were equilibrated with halite using the React module in Geochemist's Workbench (Bethke, 2013). The phrqpitz thermodynamic dataset was used. The water activity of brine equilibrated with halite was then calculated with the SpecE8 module. The mean calculated water activity in Geochemist's Workbench was 0.75 with a standard deviation <0.01.

The density of natural and anthropogenic BSF surface brines was used as an input for an equation derived from Turk's (1973) measurements of BSF brines. The average water activity calculated with method was 0.73 (standard deviation of 0.04). The maximum calculated water activity was 0.86. These results indicate that sustained surface brines at BSF have water activities between 0.73 to 0.75. A constant water activity of 0.74 was used in this research. Immediately after meteoric precipitation, BSF brine water activity is likely >0.74. Changes in water activity are buffered by dissolution of surface halite.

Penman equation evaporation

The potential evaporation calculated with the Penman equation (PE) and with the Calder and Neal (1984) water-activity corrected adaptation of the Penman equation (PE CN) are similar. The PE CN evaporation values were slightly lower (>20% less) than evaporation calculated with the unaltered Penman equation. The water activity corrected evaporation was used to create albedo-calibrated estimated evaporation values. The scaling correction values that are dependent on albedo and are used in the E_eHigh and E_eLow models are summarized in the table below.

Inputs used for albedo-calibrated estimated evaporation (E_eHigh and E_eLow) models

Albedo	*Evaporation estimation equation*	*K_c (scaling value)*
>0.37 (E_eHigh and E_eLow)	*$E_e = K_{c1}$(PE CN)/albedo*	*$K_{c1} = 0.0788$*
<0.37 (E_eHigh)	*$E_e = K_{c2}$(PE CN)/albedo*	*$K_{c2} = 0.0570$*
<0.37 (E_eLow)	*$E_e = K_{c3}$(PE CN)*	*$K_{c3} = 0.0351$*

Artificial neural network models

The MATLAB Deep Learning Toolbox (MathWorks, 2020a) was used to implement the artificial neural network used to estimate evaporation. The artificial neural network is structured such that each period is evaluated independently of the proceeding and preceding measurements. The artificial neural network consisted of two layers (a hidden training layer with 10 nodes and a single node output layer). It was trained using the Bayesian regularization backpropagation algorithm. This algorithm is implemented with the Levenberg-Marquardt optimization. The data was split randomly such that 70% of the dataset was used for training, and 30% was used for validation. Following Kelley and Pardyjak's (2019) methods, the 30-minute average values of weather station measurements were used as input values. These data were trained to replicate evaporation measured by the eddy-covariance method.

Different training inputs were used to test what inputs enhanced or decreased the quality of the artificial neural network model, as compared to the albedo-calibrated evaporation models (Figures S4 and S5). Using longwave radiation as an input improved artificial neural network evaporation outputs by making them more similar to the E_eLow model during known dry periods.

The generalizability of artificial neural network models to periods that were outside of training conditions was investigated by iteratively removing periods with low temperatures and high humidity values from the training dataset and comparing the model outputs (Figure S5). Removing lower temperatures from the training dataset led to higher evaporation estimates. This result indicates that the artificial neural network overestimated winter evaporation. This was corroborated by the difference between potential evaporation-based models of winter evaporation and the much higher winter evaporation estimates of the artificial neural network.

Text S3. Groundwater Data

Recent and historical measurements of groundwater levels, temperatures, water chemistry, anthropogenic brine fluxes, and well meta-data compiled from published data, the United States Geological Survey's national water information system (NWIS), and the Water Quality Portal are available at https://doi.org/10.5281/zenodo.4268710 (Bernau & Bowen, 2021; Kipnis & Bowen, 2018; Lines, 1978, 1979; Mason et al., 1995; Mason & Kipp, 1998; Read et al., 2017; Turk, 1973). The wells referred to in the main text as the 0.8 m and 3.5 m deep wells are identified as BLM-93C and BLM-93, respectively, in past publications. Supplemental figures incorporating current and historical groundwater data include Figures S2 and S6 to S9.

Continuous water levels from 2017 to 2021 were measured with non-vented pressure transducers. There were some data gaps from repositioning data loggers or loggers reaching data storage capacity. Groundwater levels were calculated by subtracting atmosphere pressure from the transducer-measured pressure. Where possible, groundwater measurements were corrected to be equivalent heads of a halite-saturated water column and were corrected for barometric efficiency. The effect of daily to seasonal temperature changes on groundwater level was quantified. Furthermore, the apparent specific yield of near surface sediments was estimated. The code used to perform these analyses is available at https://doi.org/10.5281/zenodo.5671739.

Equivalent head calculation

For flow calculations, head values for waters of differing density are often converted into equivalent heads of freshwater (Post et al., 2007). The water table at BSF's center is in direct contact with the evaporite crust, and is therefore halite-saturated. Therefore, to better estimate water table levels, head is estimated here by converting the measured head to an equivalent head of halite-saturated brine. The density for the 0.8 and 3.5-m deep wells was calculated using the equations' of state for these brines (Bernau & Bowen, 2021) with the soil temperature at 10 cm used as the temperature input (Figure S6). Calculated densities strongly reflected measured densities.

Although groundwater density changed throughout the year in both wells because of temperature and salinity changes, the equivalent head, when a constant density throughout the year was assumed, differed from the variable density equivalent head model by 0.5 to 1.2 cm (Figure S6). Because of this minor difference between methodologies, and the limited ground temperature and brine density measurements for many sites, groundwater density in each well was assumed to be constant when determining the equivalent head. When available, the well's brine's equation of state and a temperature range throughout the year was used to determine a representative average brine density; otherwise, the average measured density of the groundwater from a well was used.

Barometric efficiency correction

Air-pressure changes and other external forces impact water levels in wells (McMillan et al., 2019). There is differential loading of barometric pressure between the exposed well water and the aquifer's matrix and pore water in confined aquifers. This difference leads to an inverse relationship between barometric pressure and groundwater levels. The effect of air pressure on water level is quantified by a well's barometric efficiency (equation S3-1).

$$BE = 1 - \frac{dw}{db} \approx 1 - \frac{\Delta w}{\Delta b} \qquad \text{(S3-1)}$$

where barometric efficiency (BE) is equal to 1 minus the change in groundwater pressure (dw) relative to the change in barometric pressure (db). For the Bonneville Salt Flats, barometric pressure units were converted into an equivalent column of halite-saturated water. The water column measurements, reported as an equivalent head of halite-saturated brine, were then used as inputs to calculate barometric efficiency.

The median-of-ratios and linear regression time domain-based methods (as described in Turnadge et al., 2019) were used to determine the barometric efficiency BSF wells. The median-of-ratios was calculated by taking the median value of the ratio of the change in water level to the change in barometric pressure over a time period (Gonthier, 2007). The linear regression method determines the coefficient of the linear function where water level changes because of barometric pressure changes (Robinson & Bell, 1971). The time periods of change of one hour and one day were selected to test the impact of changing time period on the results.

Once the barometric efficiency was calculated it was applied to the dataset to determine what the water level would be without changes in barometric efficiency (Equations S3-2 and S3-3). The original water level and barometric efficiency corrected water level were then graphically assessed. If the application of barometric efficiency increased variability in measured water level, it was increased, in some cases to 1.

$$\Delta w_b = cumsum(((\frac{d}{dx}(b)) * (1 - BE)) \quad \text{(S3-2)}$$

where Δw_b is the change in water level originating from air pressure over the study interval relative to its starting point, $\frac{d}{dx}(b)$ is the change in air pressure (in units of an equivalent column of halite-saturated water) per unit time interval and BE is the barometric efficiency. The cumulative sum of this is calculated to determine how waster levels would change over time for changes in air pressure.

$$w_{BE} = w - \Delta w_b + mean(\Delta w_b)/2 \quad \text{(S3-3)}$$

where w_{BE} is the water level with the barometric efficiency signal removed, w is the original water level (as expressed in equivalent head of halite-saturated water). The effect air pressure on the water level at each moment is subtracted from the measured water level, because this would cause an offset in reported water elevation the mean value of the cumulative sum of water level change column is calculated and divided by two to determine the proper offset, which is added then added to the calculated water level at any moment. This methodology assumes that the barometric efficiency is invariable over time, which may not be the case for wells in unconfined aquifers.

For the 3.5 m well, the barometric efficiencies determined by the median-of-ratios and linear regression methods and with different time intervals were similar (0.59-0.61). The 0.8 m well's barometric efficiency value differed depending on if the one hour or one day time interval was used (from 0.51 to 0.86). Visual analysis of the barometric-corrected data for the 0.8 m well showed that water level data was more variable when a barometric efficiency <1 was considered; because of this, a barometric efficiency of 1 was assumed. If temperature was known to impact diurnal water levels fluctuations then only intervals of one day were used to determine well's barometric efficiency. The barometric efficiency of other BSF wells varied between 0.54 and 1. Wells screened within lacustrine sediments near BSF's center had barometric efficiencies between 0.54 and 0.60.

When the barometric correction was applied to the 3.5 m well, the resulting water level changes were similar to those observed in the 0.8 m well (Figure S6). The 3.5 m well's low barometric efficiency indicates that the lacustrine sediment-hosted aquifer in contact with the well has low permeability and poor connection with the atmosphere.

Thermal efficiency calculation and correction

Meyer (1960) first described the effect of temperature on water levels. Turk (1973) first described this effect at BSF. This effect is quantified and modeled here to identify intervals during which non-thermal processes impact water levels from seasonal to daily timescales (Figure S2).

Methodology

This methodology makes several simplifying assumptions about water levels at BSF. It assumes that the sediment column is uniform in porosity, so water level change scale linearly with temperature changes at all depths. It also assumes that temperature fluctuations are the primary control on water level changes, namely that there is no water movement in or out of the system. The effect of air pressure has also been removed by correcting for barometric efficiency. The dataset is limited to intervals that these assumptions hold. Finally, temperatures from a 10-cm depth soil probe were used as the input for these analyses to increase comparability between wells. The code used to perform these analyses is available at https://doi.org/10.5281/zenodo.5671739.

The thermal efficiency, TE (equation S3-4), was calculated by adapting the analytical framework for barometric efficiency (see prior section). The median-of-ratios was calculated by taking the median value of the ratio of the change in water level to the change in soil temperature over some time. The linear regression method determined the coefficient of the linear function where the water level changes as a function of temperature changes.

$$TE = \frac{\Delta wd}{\Delta T_{soil}} \qquad \text{(S3-4)}$$

where Δwd is the change in density and barometric efficiency corrected water depth (cm) and ΔT_{soil} is the temperature change(°C) from a 10-cm depth soil probe, and TE is the thermal efficiency.

Daily thermal efficiency values

The diurnal thermal efficiency was determined through two methods. The first method used linear regression and median-of-ratios approaches on hourly water level and temperature change periods. The second method used the median-of-ratios technique on the ratio of the daily range in soil temperature to the daily range in water level. Each month was analyzed individually using both methods to identify seasonal trends in temperature-controlled diurnal water level fluctuations.

The first method only worked with the 0.8 m deep well (BLM-93C) co-located with the soil temperature probe. This method showed that there are seasonal variations in the daily thermal efficiency. The thermal efficiency signal was strong with a high R^2 (>0.6) and a value between ~0.5 and 0.8 between May and October. This pattern reflects the correlation between diurnal water level fluctuation and maximum air temperature (Figure 6). This method was ineffective in other wells because of lags in heat transfer relating to well and water depth. Therefore, the second method was used to compare wells.

The median-of-ratios approach using daily ranges in water depth and soil temperature yielded similar results to the first method for the 0.8 m well. The median diurnal thermal efficiency of wells within the saline pan was found to be >0.25 to 0.5. The 0.8-m well was an outlier with a thermal efficiency of ~0.73. Wells to the west of the saline pan and at its northeastern edge had lower daily thermal efficiencies of 0.15 to <0.25.

Seasonal thermal efficiency values

Seasonal thermal efficiencies were determined using weekly and monthly periods of water level and temperature change. Using these more extended periods significantly limited the number of data points, so only the median-of-ratios method was used to determine seasonal thermal efficiencies. Because of the effect of non-thermal processes on water levels over these longer timescales, datasets were clipped to only the driest periods with the most notable temperature-controlled water level changes (typical August to December).

Data were plotted and then compared with observed changes in water level to qualitatively assess if calculated thermal efficiency values were recreating seasonal changes in water level. In general, seasonal thermal efficiencies replicated most groundwater changes during the dry fall months. The seasonal thermal efficiency for different wells ranged from ~0.8 to 2.2. The central areas with thicker evaporite crust had lower values, and the salt crust edge wells had higher values. Each well's diurnal and seasonal thermal efficiencies do not appear to be correlated.

Apparent specific yield of near-surface porous material

The specific yield is defined as the gravity-drainable pores within a sediment. The specific yield is often assumed to be constant within wells. However, this simplification does not apply to shallow wells and short periods because the drainage rate may take several days to years, and the water content of the capillary fringe and vadose zone, and antecedent conditions can vary greatly and influence measurements (Crosbie et al., 2019). Because of this, the apparent specific yield (S_{ya}) is often reported. This value factors in the effect of the capillary fringe, and it begins to approach zero as the groundwater level approaches the surface. Only at deeper groundwater depths does S_{ya} approach a sediment's specific yield (Crosbie et al., 2005; Duke, 1972).

Specific yield is highly dependent on environmental conditions and sediment texture (Healy & Cook, 2002). As Healy and Cook (2002) note, the value of Sy to use for a study can be unclear. Because of the low topography at BSF and its well-constrained precipitation and evaporative fluxes, the apparent specific yield of the shallow crust at BSF was estimated using a form of the water budget equation which relies on water table fluctuations (Gerla, 1992; Lv et al., 2021; Walton, 1970) (equation S3-5).

$$S_{ya} = \frac{\frac{\mathrm{PPT}+\mathrm{Q}_{on}-\mathrm{Q}_{off}-\mathrm{ET}-\Delta\mathrm{S}^{sw}\mathrm{sw}-\Delta\mathrm{S}^{uw}}{\Delta wd}}{\Delta t} \qquad \text{(S3-5)}$$

where PPT is precipitation, Q_{on} and Q_{off} are surface and subsurface water flow in and out of the area of interest, ET is evapotranspiration, ΔS^{sw} is surface water storage, ΔS^{uw} is unsaturated zone water storage, Δwd is the change in groundwater height, and Δt is the study period. Q_{on}, Q_{off}, ΔS^{sw}, and ΔS^{uw} were assumed to be negligible because of the study site's low topography and hydraulic gradients and its near-surface water table with a capillary fringe can intersect the surface. Only dry periods with no surface water at the beginning of the interval were used. This equation then simplifies to:

$$S_{ya} = ((\mathrm{PPT} - \mathrm{E}_e)/\Delta wd)dt \qquad \text{(S3-6)}$$

where over a period dt the change in groundwater height (Δwd) is attributable to the net recharge ($PPT - E_e$). More simply, this is the ratio of infiltrated precipitation to the change in the water table. This calculation assumes that recharge is the only variable influencing water level. To address this concern, only daily averages of water levels that were corrected for barometric efficiency were

considered were considered to partially eliminate the influence of temperature and air pressure fluctuations upon water levels.

The daily average value of water level, reported as the equivalent height of saturated water column and corrected for barometric efficiency (for the 3.5 m well), was used to compensate for these variables. Furthermore, the input periods to calculate S_{ya} were selected to meet the following criteria **1)** *initial water depth greater than 6 cm,* **2)** *recharge $(PPT-E_e)/E_e > 0.5$, and* **3)** *the final water depth was below the surface and did not decline rapidly in the days after precipitation (which would be indicative the reverse Wieringermeer or Lisse effects, where trapped air increases the apparent water column (Gillham, 1984; Heliotis & DeWitt, 1987)). Furthermore, to reduce to impact of the Lisse effect, apparent specific yield values less than 0.03 were not considered.*

If these conditions were met more frequently, a threshold value of >5mm of precipitation would also be included for determining S_{ya} criteria. The study intervals used here extended one day before precipitation to at least one day following precipitation. Some periods include several precipitation events.

The S_{ya} values determined by this method varied (mean of 0.09 with a standard deviation of 0.04).

Apparent specific yield relative to prior BSF research

The porosity and characteristics of evaporite crust at BSF have been previously described and indicate that the apparent specific yield reported here is reasonable. The porosity of upper halite crust samples from X-ray computed tomography measurements was determined to be 29% (±5%) (Bernau & Bowen, 2021). Porosity was also estimated from the dry density of crystalline crust from 30 samples reported by Mason & Kipp (1998). Assuming an 80-20 ratio of halite to gypsum in these samples yields an average estimated porosity of 23%. Using other proportions of halite to gypsum leads to a range of estimated porosities of 19 to 40%. Halite-rich portions of the lower part of the evaporite crust have an estimated porosity of 35-45% (Bernau & Bowen, 2021). The porosity of fine to medium sand in gypsum layers is likely between 20-50% (Bowen et al., 2018). Past examination of the fine-grained lacustrine sediments at BSF suggests a porosity of 50% and a specific yield of 10% (Turk et al., 1973).

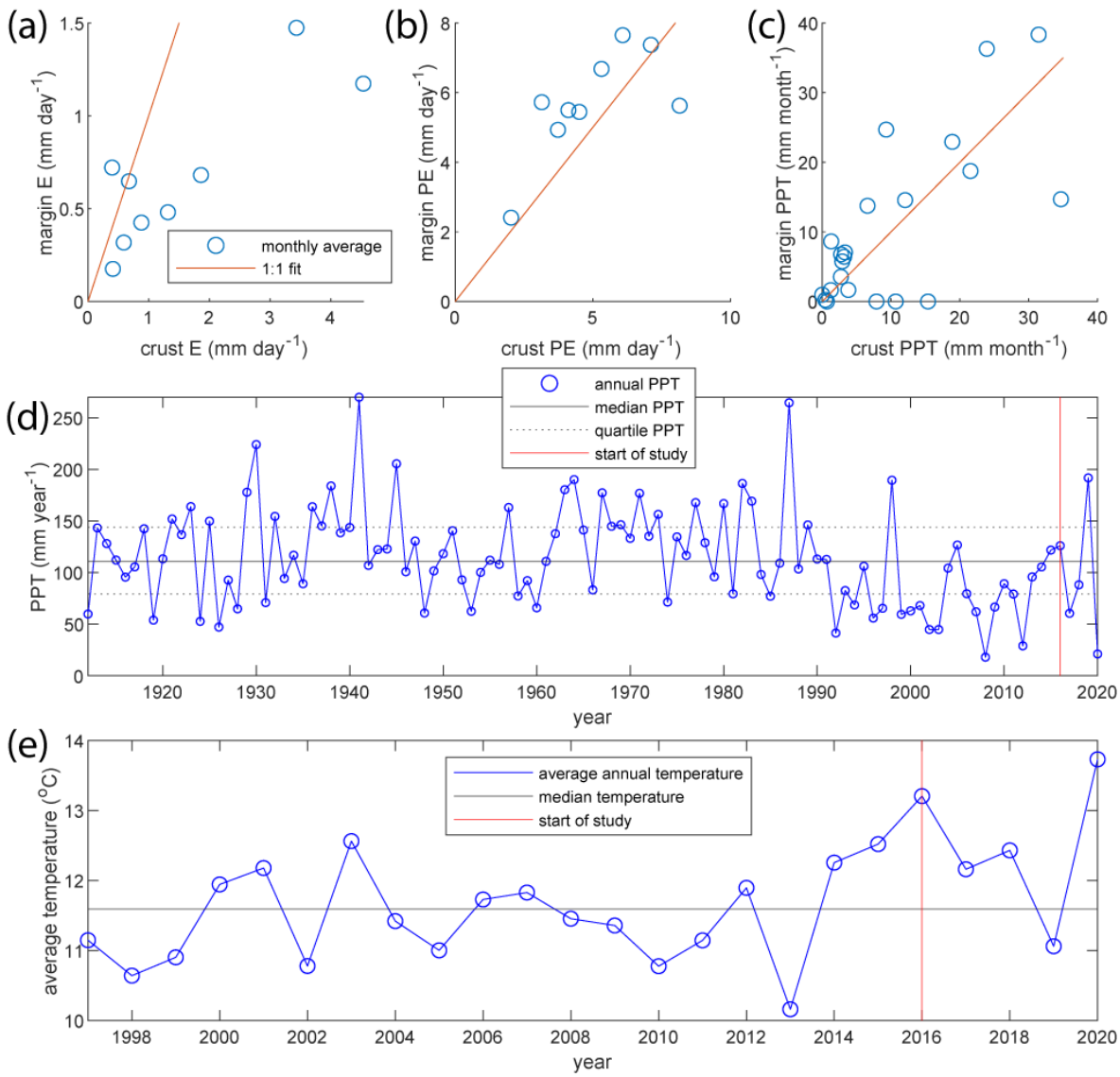

Figure S1. *Long-term climate measurements from Wendover, Utah, and comparisons of monthly average values of evaporation and potential evaporation, and monthly sums of precipitation at the western margin (margin) and center (crust) of the Bonneville Salt Flats from April to October 1993 and April to August 1994. (a) Crust evaporation (E) was higher than playa margin evaporation. (b) Potential evaporation (PE) was higher at the playa margin. (c) Cumulative precipitation (PPT) between the crust and the margin was within 5% of each other from October 1992 to July 1994. (d) Wendover, Utah, annual precipitation record demonstrates that the study period was drier than average but included unusually wet and dry years and that there has been a long-term decline in precipitation. (e) Average annual temperatures from Wendover, Utah, reveal that the study period was warmer than average. (Figure data from Mason & Kipp, 1998; NOAA Climate Data Online Portal and MesoWest).*

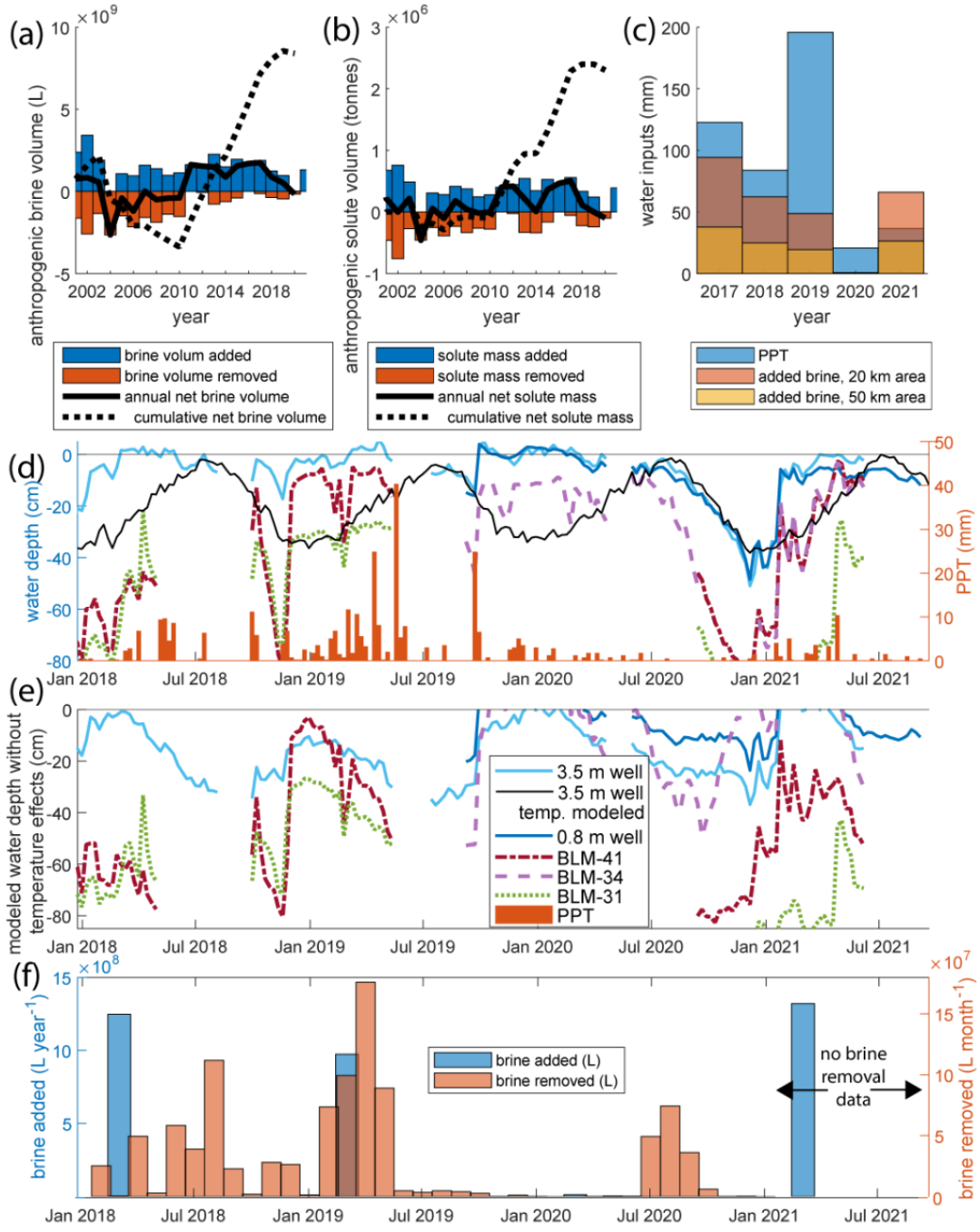

Figure S2. *Anthropogenic brine volumes and solute mass balances over time in comparison to precipitation and limited groundwater level measurements. (a) Net annual BSF anthropogenic brine volumes since 2001. (b) Mass of anthropogenic solutes added and removed from BSF (updated from Kipnis & Bowen, 2018). (c) Millimeters of water added to southwestern area of BSF annually, assuming added brine covers an area between 20 and 50 km2 (as suggested by Bowen et al., 2017). (d) Density-corrected changes in groundwater level over time (key in (e)). Wells BLM-41, BLM-34, and BLM-31 are located near brine extraction ditch. The black line shows temperature-controlled water levels in the 3.5 m well if no water inputs or output is assumed. (e) Modeled groundwater changes over with temperature effects on water levels removed. (f) Monthly values of brine addition and removal during study period.*

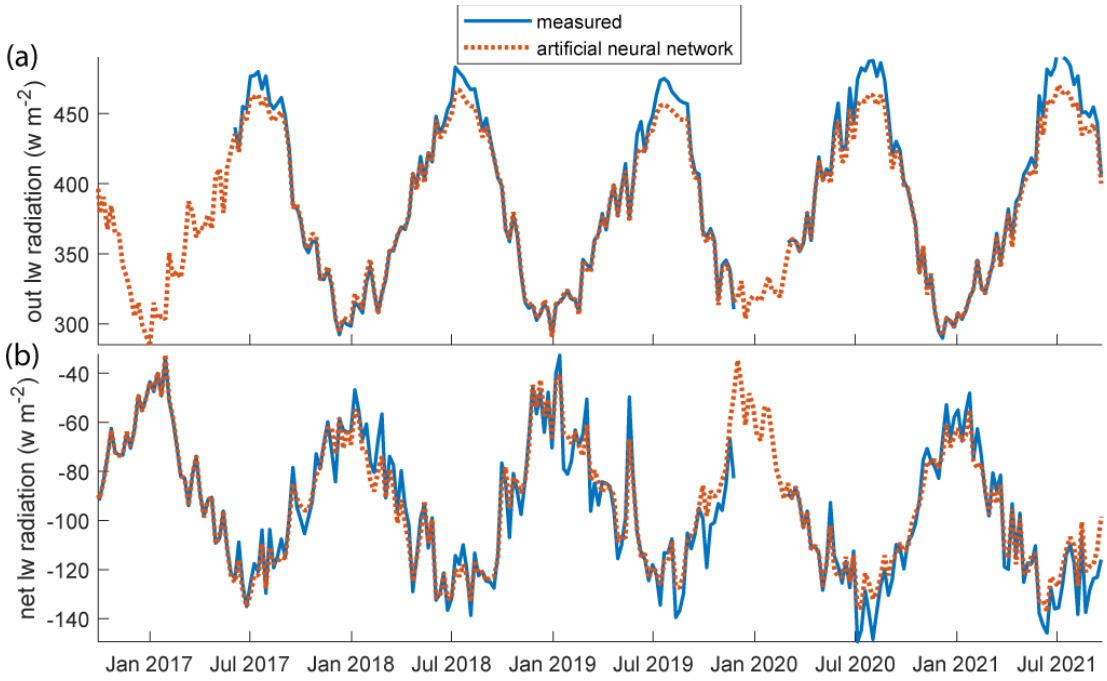

Figure S3. *Weekly average values of (a)outgoing longwave (lw) radiation and of (b) net lw radiation.*

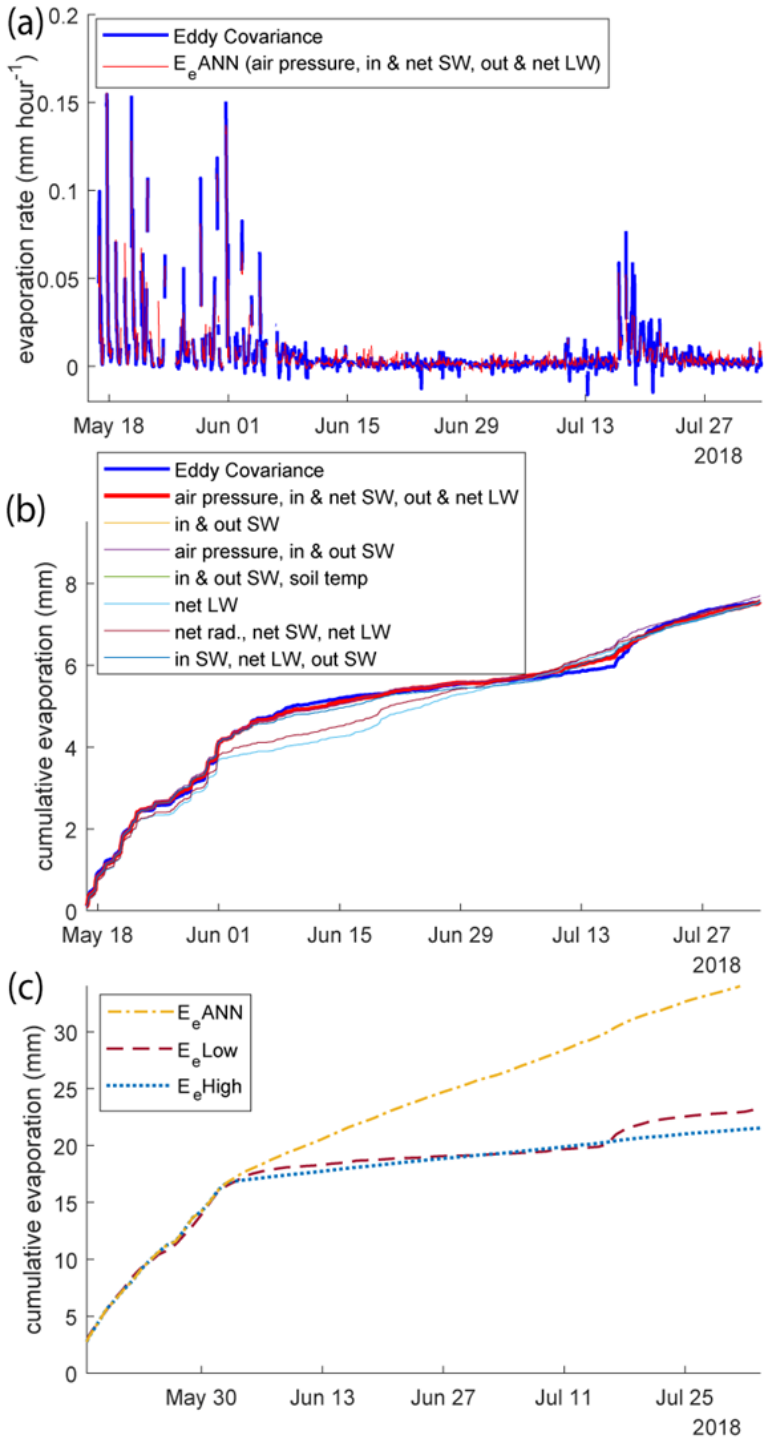

Figure S4. *Eddy-covariance evaporation values used for training compared with artificial neural network evaporation values (model inputs in addition to air temp, relative humidity, wind speed, and time of day denoted in legends with LW and SW referring to radiation). (a) Hourly evaporation rates from eddy-covariance measurements and the artificial neural network. (b) Comparison of cumulative evaporation measurements between eddy-covariance data and different artificial neural networks. (c) Calibration period cumulative values of estimated daily evaporation made with different methods. (b) and (c) period totals differ because of data gaps in (b).*

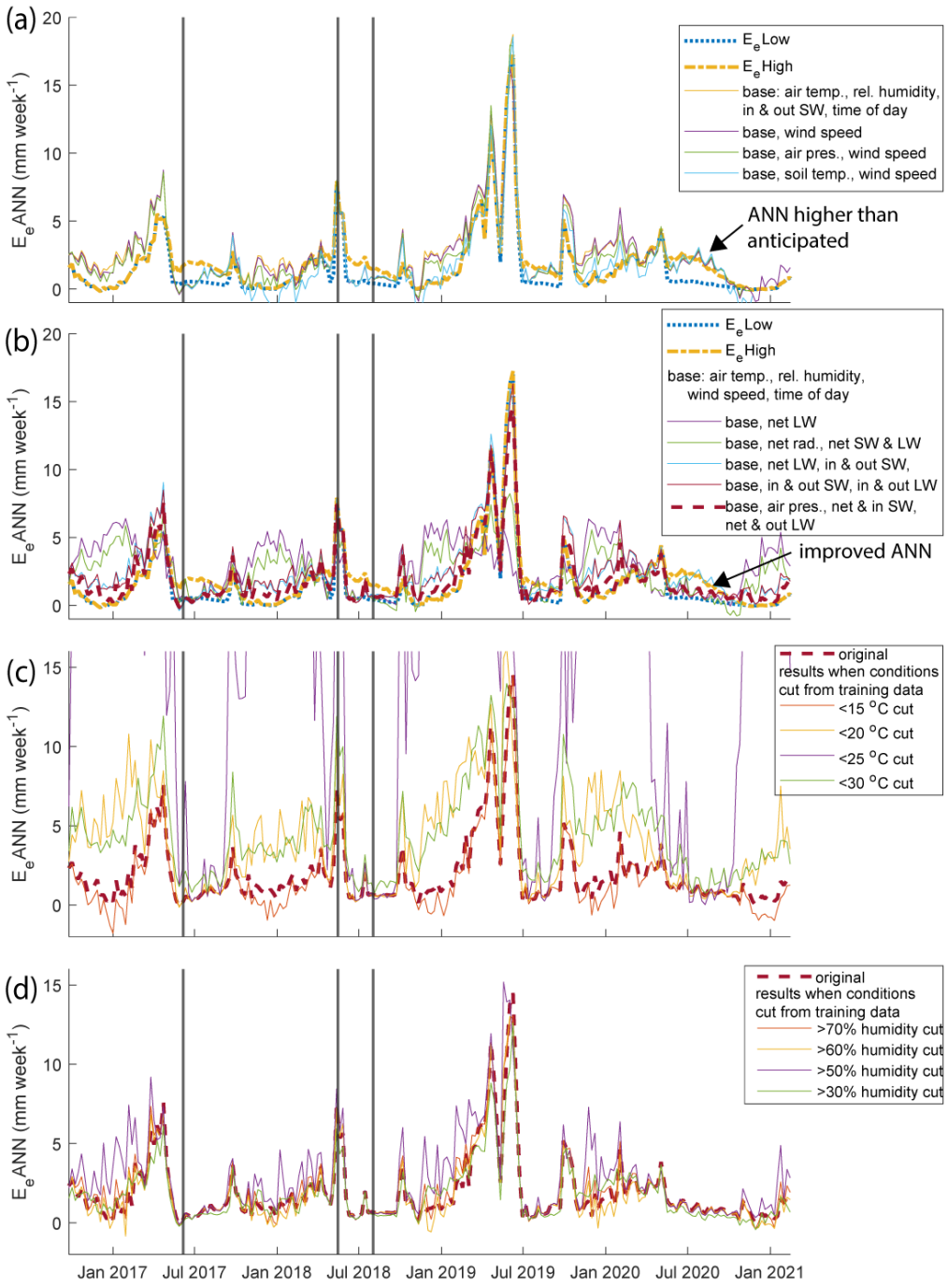

Figure S5. *Comparison of the median values of evaporation modeled with select artificial neural networks. (a-b) Estimated evaporation trained with different inputs (base inputs are described in key, with additional inputs noted). Estimated evaporation made with albedo-calibrated Penman evaporation models shown for comparison. A smaller number of inputs without longwave radiation are used in (a), while longwave radiation values are used in (b). (c-d) The impact of removing incrementally lower humidity and higher temperature periods from the training dataset on artificial neural network evaporation estimates. (c) Winter evaporation estimates were much higher when lower temperatures are removed from the training dataset. (d) Removing high humidity values from the training dataset had minimal effects on evaporation estimates.*

Figure S6. *Groundwater equivalent head correction. (a) Measured (filled circles) and calculated (lines) groundwater densities in 0.8 and 3.5 m deep wells. (b) Comparison of measured water depth and halite-saturated water equivalent head from 0.8 and 3.5-m wells. (c) The difference between head calculated with a constant density and head calculated with a variable density is between 0.5 and 1.2 cm. (d) Centimeters of difference in head between the 3.5 and 0.8-m deep wells show vertical flow gradients vary seasonally.*

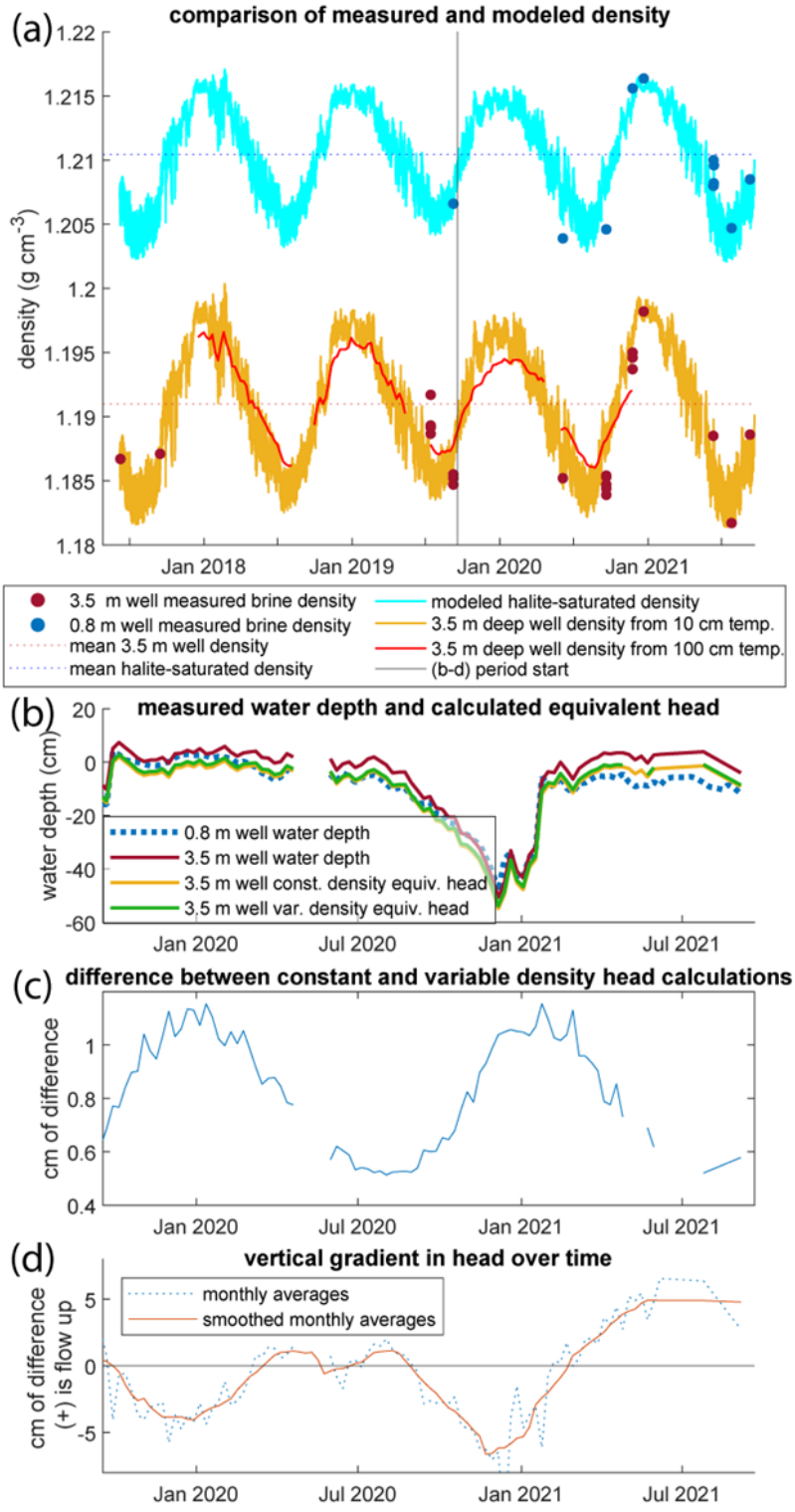

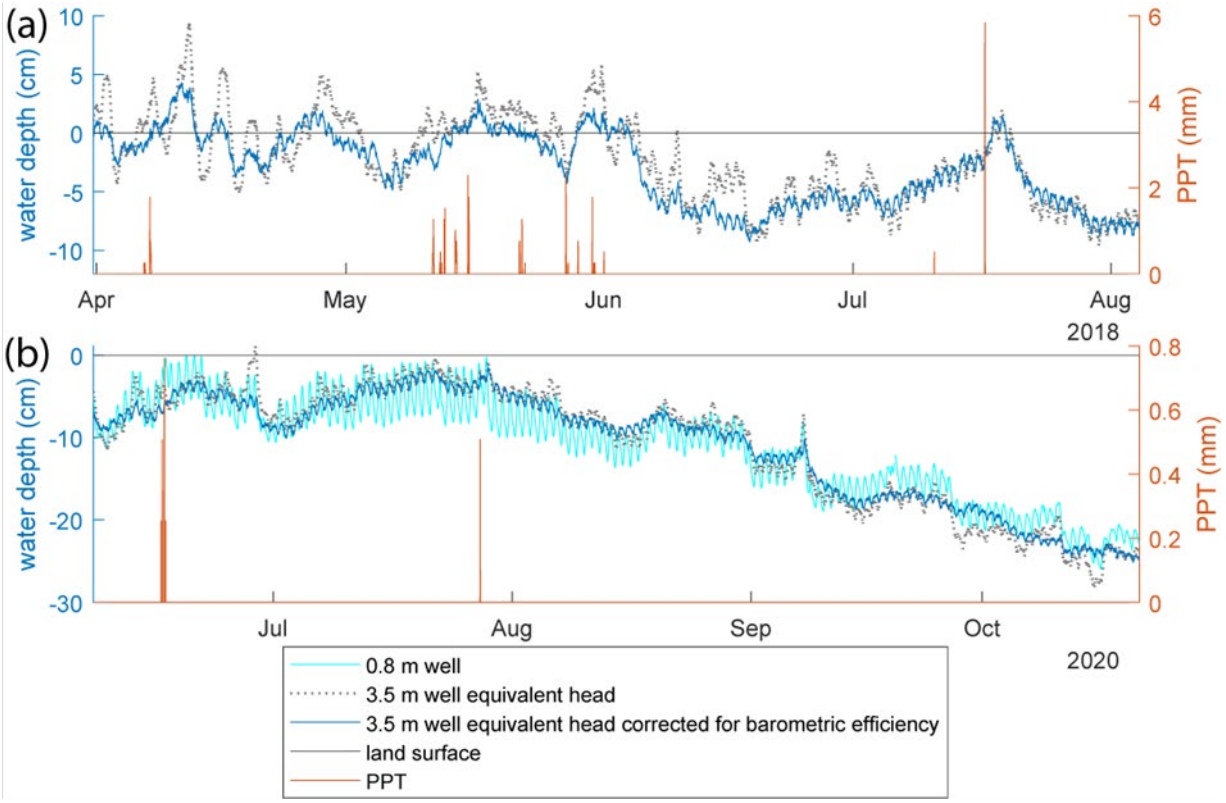

Figure S7. *Equivalent halite-saturated head and equivalent halite-saturated head corrected for barometric efficiency in the 3.5 m well. Precipitation shown for reference. (a) Barometric correction removes significant variability from the water level, making it more representative of the water table in the halite crust. (b) Comparison of corrected values and measured water table level in shallow surface (0.8 m well) demonstrates agreement between barometric-corrected head and observed near-water table water level values.*

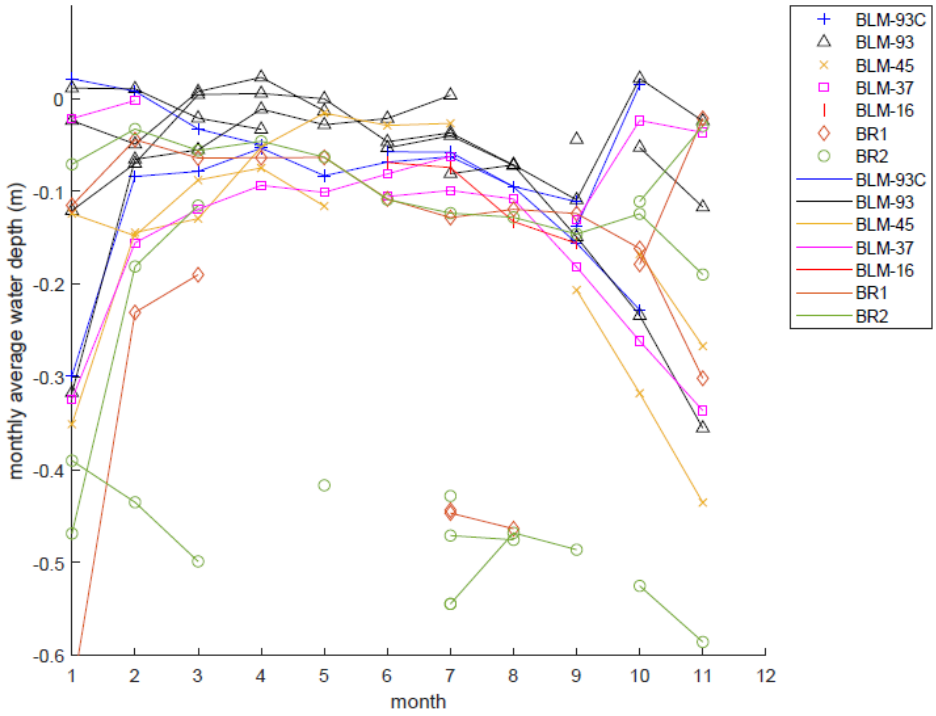

Figure S8. *Average monthly groundwater depths (corrected to equivalent head of halite-saturated brine) from wells along the centerline of the Bonneville Salt Flats, where the water table is consistently high (Lines, 1979; Mason & Kipp, 1998; Turk, 1973; and USGS water data portal). (BLM-93 and BLM-93C are the same wells as the 3.5 and 0.8 m well described in this paper). These measurements illustrate that water levels stabilizes in July to August. Other months of the year are more variable. The lower summer of 1967 water levels in BR1 and BR2 (Turk, 1973), are from when the Salduro Loop water collection ditch was active. Groundwater collection rates from this time are unknown.*

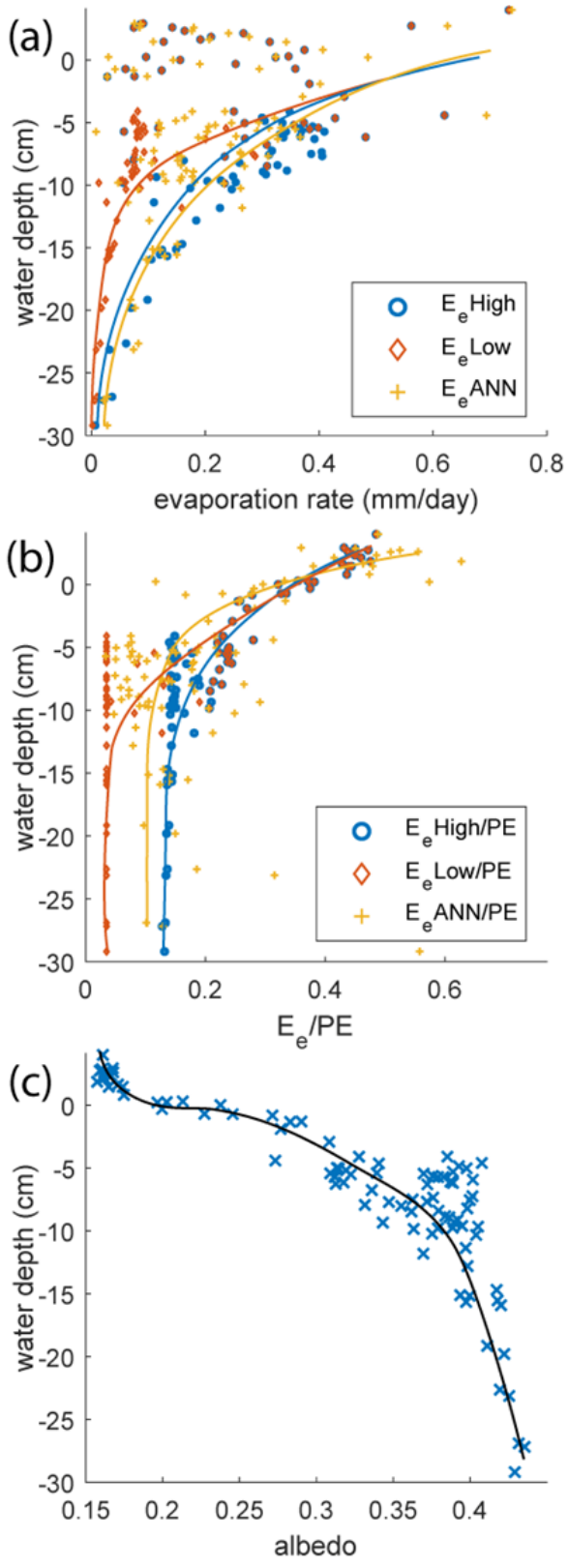

Figure S9. *Relationship between water depth in the 0.8 m well and (a) evaporation rate, (b) evaporation relative to potential evaporation, and (c) albedo.*